

# The Structure Sensitivity of $H_xMoO_3$ Precipitation on $MoO_3(010)$ during Reactions with Methanol

Richard L. Smith and Gregory S. Rohrer<sup>1</sup>

Carnegie Mellon University, Department of Materials Science and Engineering, Pittsburgh, Pennsylvania 15213-3890

Received May 29, 1998; revised September 30, 1998; accepted January 25, 1999

Atomic force microscopy has been used to examine the effect of surface morphology on the formation of  $H_xMoO_3$  during the reaction of  $MoO_3$  with methanol. By heating  $MoO_3$  crystals in hydrous environments, pits can be formed on the (010) surface. We have found that pit formation is activated by elastic strain from extended defects and because of this, it is possible to exercise some degree of control over the density, crystallography, and size of these features. This phenomenon was exploited to create different and well characterized morphological features on pairs of mated surfaces, cleaved from the same single crystal. The mated pairs were then reacted simultaneously in methanol- $N_2$  mixtures at temperatures between 300 and 330°C. Surfaces with pits that expose  $\{h0\}$  type facets containing undercoordinated Mo sites were observed to intercalate more H than relatively flat surfaces. This result, together with the observation that acicular  $H_xMoO_3$  precipitates grow from the edges of the pits, suggests that the undercoordinated surface Mo on the  $\{h0\}$  surfaces are active for the dissociative chemisorption of methanol at temperatures between 300 and 330°C. © 1999 Academic Press

**Key Words:** molybdenum trioxide; partial oxidation; surface structure; atomic force microscopy.

## INTRODUCTION

The first step in the oxidation of methanol (MeOH) by  $MoO_3$  is thought to be the dissociative chemisorption of the alcohol at an undercoordinated surface Mo site (1–3). This chemisorption step leaves a hydroxyl group and a methoxy group bound to the surface. In the presence of oxygen, the methoxy decomposes to form formaldehyde and hydrogen. The liberated hydrogen combines with a hydroxyl to form water, which then desorbs and leaves behind a surface oxygen vacancy (4). In the absence of oxygen, MeOH is converted to a combination of products including hydrogen, methane, and dimethyl ether (4), while the catalyst intercalates hydrogen to form  $H_xMoO_3$  precipitates (5–7). The formation of  $H_xMoO_3$  precipitates on the (010) surface can be directly observed by atomic force microscopy (AFM), visible light microscopy, and X-ray diffraction (7). Consid-

ering the fact that the surface methoxy does not decompose to formaldehyde in the absence of oxygen, the hydrogen that intercalates into  $MoO_3$  must be formed during the initial dissociative chemisorption of the alcohol. Therefore, the amount of  $H_xMoO_3$  formed at the surface provides a quantifiable indicator of MeOH chemisorption.

The objective of the experiments described in this paper is to observe how different crystal terminations and densities of undercoordinated Mo sites influence the rate of  $H_xMoO_3$  precipitate formation and, therefore, MeOH chemisorption. The potential sources of undercoordinated surface Mo can be identified by considering the anisotropic structure of  $MoO_3$  (8). The  $\alpha$ - $MoO_3$  structure is composed of layers of corner- and edge-sharing  $MoO_6$  octahedra stacked along the [010] direction (see Fig. 1). The octahedral groups link by corner sharing along [100], edge sharing along [001], and van der Waals forces hold the layers together along [010]. In Fig. 1, note that oxygen terminated {010} surfaces can be formed by cleavage at the van der Waals gap without breaking any primary Mo–O bonds. Therefore, the Mo maintains its bulk octahedral coordination and the only possible undercoordinated Mo atoms on an ideally planar (010) surface are adjacent to O vacancies. However, all real surfaces contain some steps and the edges of steps on {010} surfaces will have local bonding geometries similar to lateral  $\{h0\}$  facets. For example, creation of a (100) surface (or a step along the [001] direction) requires breaking one of the Mo–O bonds in each bridging Mo–O–Mo unit across the interface. For every Mo–O–Mo linkage broken, one Mo will be exposed in a five-coordinate site, while the other will remain octahedrally coordinated. Therefore, the Mo on this surface have an average coordination number of 5.5. To create a (001) surface or step along [100], two Mo–O–Mo links must be broken, leaving the exposed Mo with an average coordination number of 5. From this geometric point of view, the Mo atoms on a general  $\{h0\}$  surface or  $\langle h0 \rangle$  step have an average coordination number between 5 and 5.5. In summary, based on a broken bond model, Mo atoms on  $\{h0\}$  faces and step edges have a lower average coordination number than those on the {010} surfaces.

<sup>1</sup> To whom correspondence should be addressed. Fax: (412)268-7596. E-mail: gr20+@andrew.cmu.edu.

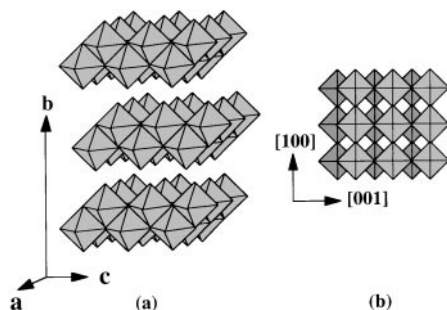


**FIG. 1.** Polyhedral representation of the  $\text{MoO}_3$  structure.  $\text{MoO}_3$  has a primitive orthorhombic cell (Pbnm) and its lattice parameters are  $a = 3.963 \text{ \AA}$ ,  $b = 13.856 \text{ \AA}$ ,  $c = 3.6966 \text{ \AA}$ . (a) An oblique projection. (b) A projection on the (010) plane. The polyhedra with the darker shading are in a lower plane.

The concentration of undercoordinated surface Mo arising from oxygen vacancies is thermodynamically controlled and limited. In  $\text{MoO}_3$ , the oxygen vacancy concentration,  $[V_{\text{O}}]$ , increases with increasing temperature and/or diminishing partial pressure of oxygen. For very low oxygen partial pressures, an upper limit for  $[V_{\text{O}}]$  is established by the formation of crystallographic shear planes or reduced phases. While definitive data concerning the limiting oxygen vacancy concentration in  $\text{MoO}_3$  are not available, Bursill's (9) work suggests that the limiting concentration per O site is  $\ll 10^{-3}$  and estimates of the concentration in reducing environments at temperatures of 300 to 330°C are on the order of  $10^{-4}$  (10). Assuming this to be true and taking the concentration of Mo just below the (010) surface to be  $(ac)^{-1} = 6.8 \times 10^{14}/\text{cm}^2$ , then the maximum number of active sites associated with oxygen vacancies is  $6.8 \times 10^{10}/\text{cm}^2$ . The concentration of undercoordinated Mo sites due to the presence of steps, on the other hand, is variable and depends on surface preparation. Based on AFM data, the total length of single layer steps per unit (010) surface area is on the order of  $2 \times 10^3/\text{cm}$  (11). Taking the density of Mo along such a step to be  $2.7 \times 10^7/\text{cm}$ , the density of active sites due to steps is  $5 \times 10^{10}/\text{cm}^2$ . Therefore, for a typical (010) facet at 330°C, the concentrations of undercoordinated surface Mo sites arising from oxygen vacancies and steps are comparable.

There is, however, an important distinction between the active sites arising from these two sources. While the concentration of undercoordinated surface Mo associated with oxygen vacancies is fixed and limited, the undercoordinated sites arising from steps can be controlled. In earlier publications, we have described the conditions under which pits form and change shape on the  $\text{MoO}_3$ (010) surface (12, 13). Based on the geometric arguments presented in the previous paragraphs, the pits must be bounded by undercoordinated surface Mo and the density of such sites increases with the width and depth of the pits. In the present paper, we show that pit formation is activated by elastic strain from

extended defects and that because of this, we are able to exercise some degree of control over the density, crystallography, and size of these features. Furthermore, by determining the density and configuration of  $\text{H}_x\text{MoO}_3$  precipitates which form on (010) surfaces with different populations of undercoordinated surface Mo sites during reactions in  $\text{MeOH-N}_2$  mixtures at  $\sim 330^\circ\text{C}$ , we are able to quantify the influence of these sites on the chemisorption process.

## METHODS

### (a) Sample Preparation

Single crystals of  $\alpha\text{-MoO}_3$  were grown by a previously described chemical vapor transport technique (14). The single crystal samples were reacted at atmospheric pressure in a quartz reaction tube (i.d. = 19 mm) with a 0.3-m hot zone. The temperature at the center of the hot zone was monitored with a type-K thermocouple which was completely enclosed in a glass sheath. The  $\text{MoO}_3$  crystals were cleaved in the ambient with a razor blade, placed in a silica boat, and loaded into the cold zone of the quartz reaction tube. With the hot zone of the reactor at temperature, the system was purged three times by alternately evacuating and back-filling with the reactant gas mixture of interest. The silica boat holding the sample, which was attached to a quartz magnetic transfer rod by chromel clips, could be moved into and out of the hot zone under a continuous flow of gas without exposure to the ambient.

### (b) Pit Formation Reactions

Pits were introduced on the  $\text{MoO}_3$ (010) surface by reducing single crystal samples in a 250 cc/min flow of as-received forming gas (10%  $\text{H}_2\text{-N}_2$  w/ $\sim 20$  ppm  $\text{H}_2\text{O}$ ) at 400°C. Crystals were reduced either alone in the silica boat or with a small piece of Ta foil ( $1 \times 10 \times 0.1$  mm) which acts as an oxygen getter. Pits formed by this reducing treatment were elongated along the  $\langle 101 \rangle$  direction. Reoxidation treatments were carried out in the same reactor, with the ends of the tube open to the ambient atmosphere, to enlarge and reorient the pits. Pits treated in oxidizing atmospheres were oriented in the  $\langle 001 \rangle$  direction.

### (c) Reactions with MeOH

The reactions with  $\text{MeOH-N}_2$  mixtures were carried out between 300 and 330°C in a 150 cc/min flow of gas at atmospheric pressure. The  $\text{N}_2$  carrier gas was dried by passing it through a column of  $\text{CaSO}_4$  (Drierite) and then saturated with  $\text{MeOH}$  (99.9%, Aldrich) in a bubbler at 0°C or room temperature ( $25 \pm 1^\circ\text{C}$ ). Following reaction, the samples were transferred to the cold zone and cooled to room temperature under a flow of  $\text{MeOH-N}_2$ . No special precautions were taken to prevent exposure of the samples to the ambient between pit formation and subsequent reaction with  $\text{MeOH}$ .

## (d) AFM Analysis

After the reacted samples were cooled to room temperature, they were momentarily exposed to the ambient before they were transferred to a glove box in which a Digital Instruments Nanoscope SPM was operated. The Ar atmosphere in the glove box contained less than 5 ppm of  $\text{H}_2\text{O}$  and  $\text{O}_2$ . The AFM was operated in contact mode using pyramidal  $\text{Si}_3\text{N}_4$  cantilevered tips and forces between 0.1 and 8 nN. Control experiments, in which the samples were transferred directly to the glove box without exposure to the ambient, have demonstrated that exposing the surface to the ambient for up to 1 day does not alter the surface structure of the crystals reacted with MeOH in any manner detectable with AFM. A first- or second-order plane was subtracted from all of the images presented in this paper. In some cases, the images were cropped from larger scans to exclude edge artifacts and the plane subtraction was applied in a line-by-line mode.

$H_x\text{MoO}_3$  precipitates form topotactically in the  $\text{MoO}_3$  matrix during the reactions with MeOH- $\text{N}_2$  and, because they protrude from the surface, are easily detected in topographic AFM images (7). We assume that one H is removed during the chemisorption of each methanol and that one possible path for this H is to react with  $\text{MoO}_3$  to form  $H_x\text{MoO}_3$ . The amount of  $H_x\text{MoO}_3$  is therefore assumed to be a relative quantifiable measure of alcohol chemisorption. To quantify the amount of  $H_x\text{MoO}_3$  formed during any given reaction, we estimate the total volume of the phase in a given surface area,  $V_H$ . For example, the AFM image in Fig. 2a shows a typical precipitate and its lateral dimensions. We idealize the precipitate's shape as a diamond elongated along  $\langle 203 \rangle$  whose area in the (010) plane is one half of the product of its length ( $l$ ) and width ( $w$ ), as illustrated in Fig. 2b. The thickness of the particle is estimated based on the measured surface relief ( $h$ ) and X-ray diffraction data which shows that the [010] axis of the precipitate phase is 0.2 Å larger than that of the matrix phase (7). Assuming that all of the strain between the precipitate and the matrix is relieved at the free surface, then the number of unit cells transformed is the measured height divided by 0.2 Å (see Fig. 2c). This number, multiplied by the length of the [010] axis of the precipitate (14.05 Å), gives the particle thickness,  $t$ . The volume of any given particle is then calculated as one half of the product of its length, width, and thickness. The volume of  $H_x\text{MoO}_3$  per unit surface area is calculated by summing all of the particle volumes in an image and dividing by the observed area.

We should mention that several errors are introduced by this procedure. First, the finite size of the AFM tip leads to a systematic overestimation of the particle volume. Considering that the features described here are much wider than they are high, this overestimation is negligible for most of the precipitates. However, for those with dimensions less than 100 nm, the details of the tip shape can become sig-

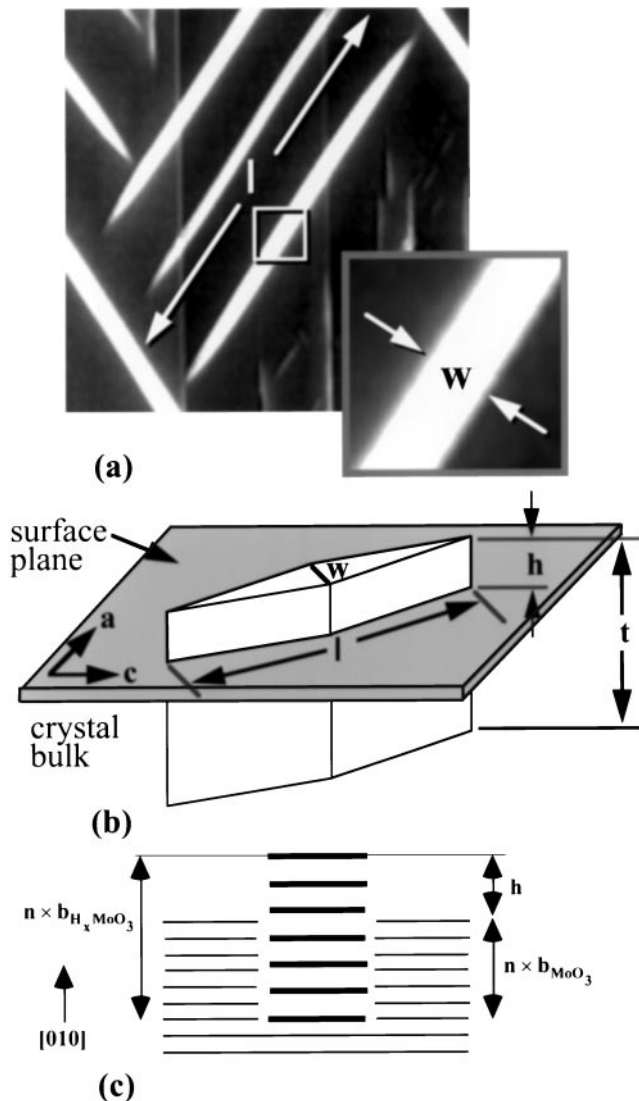


FIG. 2. (a) A typical AFM image of an  $H_x\text{MoO}_3$  precipitate formed at the  $\text{MoO}_3(010)$  surface during reactions with MeOH. The lateral dimensions ( $l$  and  $w$ ) of the precipitates are determined directly from AFM images. The dimension of this particular precipitate are  $l = 25 \mu\text{m}$ ,  $w = 950 \text{ nm}$ , and  $h = 10 \text{ nm}$ . (b) Idealized model for the habit of the  $H_x\text{MoO}_3$  precipitate. (c) Schematic illustration of the geometric relationship between the  $H_x\text{MoO}_3$  precipitates and the  $\text{MoO}_3$  matrix. The difference in the interlayer spacings of the precipitate and the  $\text{MoO}_3$  matrix are not drawn to scale.

nificant. While we have made no attempt to correct for this effect, we also note that for any two surfaces where quantitative numerical comparisons are made, the observations were recorded with the same probe. Therefore, the magnitude and sign of the error is the same in both cases. There is an additional error in the magnitude of the measured volumes that derives from our simplified view of the particle's shape. However, since the sign of the error should always be the same, it affects only the absolute values of the volumes. The reliability of the relative values rests only on the existence of a common particle habit.

## RESULTS

*(a) Pit Formation on the (010) Surface*

In an earlier report, we demonstrated that when the (010) surface is reduced with 10%  $\text{H}_2\text{-N}_2$  above  $350^\circ\text{C}$ , pits form on the originally flat surface (12). While the pits are initially small (30 Å deep and several hundred Å wide) and circular in shape, the depth and width increase with longer reaction times and the long axis becomes nearly parallel to  $\langle 101 \rangle$ . Experiments in different gases showed that pit formation was associated with the presence of water vapor, which is known to enhance the sublimation of  $\text{MoO}_3$  through the formation of volatile molybdenum oxyhydroxides such as  $\text{MoO}_2(\text{OH})_2$  (14, 15). More recent experiments suggest that water vapor is a necessary, but not sufficient, condition for the pit formation process. For example, when crystals are

heated in oxidizing atmospheres containing water vapor at the same temperature, the pit formation process can be detected only at the positions where extended defects, such as screw dislocations, intersect the surface. The images in Fig. 3 show the surface of a crystal heated for 3.5 h in air at  $400^\circ\text{C}$ . The descending, spiral steps are each 7 Å high and a Burgers circuit around the central point in each image shows that dislocations with screw components of 7 and 14 Å intersect the surfaces shown in Figs. 3b and 3c, respectively.

When one considers the amount of material removed from each pit, it is clear that the volatilization is accelerated at these surface/dislocation intersections by the elastic strain around the defect. Since the elastic strain energy around a dislocation line is proportional to the square of the Burgers vector, the driving force to remove material from the dislocation etch pit in Fig. 3c should be four times

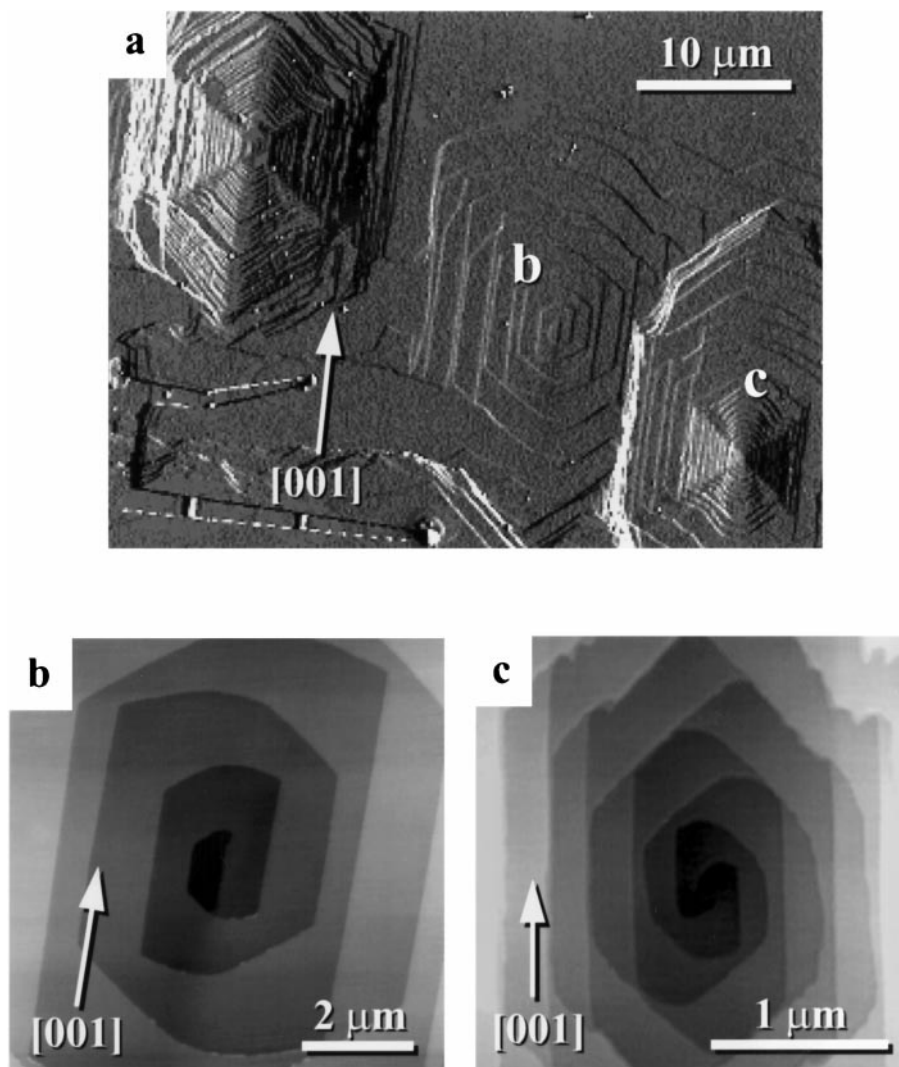


**FIG. 3.** (a) AFM deflection image of a group of dissolution spirals on the  $\text{MoO}_3(010)$  surface. The center spiral, b, is a partial dislocation with a Burgers vector of 7 Å, while the spiral labeled c is a unit dislocation with a Burgers vector of 14 Å. Higher resolution AFM topographs of these two dislocations are shown in (b) and (c).

that of the one in Fig. 3b. Measuring the lateral dimension of the terraces surrounding the defect cores verifies that the pit in Fig. 3c is four times deeper than the one in Fig. 3b.

By counting the dislocation etch pits on several crystals, we have measured an average dislocation density of  $1.5 \times 10^4/\text{cm}^2$ . Because the volatilization reaction is limited to these relatively rare sources of elastic strain, the observed sublimation rates in humid oxidizing atmospheres are relatively low. On the other hand, pit densities as high as  $10^9/\text{cm}^2$  can be formed when the surface is reduced in the presence of water. In this case, the crystallographic shear (CS) plane defects which form to compensate O loss provide an abundant source of elastic strain. When images with sufficiently high resolution are examined, we find that the 1.5-Å steps that are characteristic of surface/CS plane intersections invariably intersect the pits (see Fig. 4). Furthermore, the high pit densities are observed only at temperatures above 350°C, where CS planes begin to form (12, 17).

Based on our observations, the two necessary conditions for pit formation at 400°C are water vapor and elastic strain from extended defects such as dislocations or CS planes. Because surface/dislocation intersections are rather infrequent, volatilization rates in oxidizing conditions are much lower than in reducing conditions where CS planes form. This observation implies that the density of surface pits should correlate with the density of CS planes and the partial pressure of oxygen in the reactor. In support of this idea, we find that the presence of an oxygen getter such as Ta in-

fluences the pit formation process. When Ta is present in the reactor, CS planes and pits form homogeneously across the entire (010) surface during a 5-min treatment at 400°C. When crystals are reacted without Ta, however, reduction proceeds inhomogeneously and is favored at the edges of the crystal. After 5 min at 400°C, the center of the crystal is indistinguishable from the fresh cleaved surface with AFM. However, within approximately 100  $\mu\text{m}$  of the edges of the crystal, the population of CS planes and surface pits is comparable to that found on the surfaces of samples reduced in the presence of Ta for an equivalent period of time. These observations, combined with tantalum's well known ability to scavenge O, lead us to conclude that the partial pressure of oxygen is reduced below that which would be established solely by the  $\text{H}_2$ - $\text{H}_2\text{O}$  equilibrium. Thus, as the driving force for reduction is increased, so are the kinetics of the CS plane and pit formation process.

We have found that the most homogeneous population of pits is formed by reducing crystals for a short period of time ( $t \leq 10$  min) in forming gas at 400°C in the presence of Ta and then oxidizing the samples in air for a longer period ( $t \geq 1$  h) at the same temperature. Annihilation of CS planes occurs much more slowly than creation, so even after relatively long anneals, the pits continue to grow (although more slowly than in the reducing conditions). Furthermore, during annealing in air, they take on a rectangular shape with the long axis oriented along  $\langle 100 \rangle$  (13). Finally, we note that it is often impossible to completely remove all of the CS planes and, at the same time, produce the desired pit population. Thus, the stoichiometry of the crystal must often be compromised in order to tailor the surface morphology.

#### (b) $H_x\text{MoO}_3$ Formation on Pitted Surfaces

The objective of this study was to compare the amount of  $H_x\text{MoO}_3$  formed on surfaces that were identical in every respect except for the density of undercoordinated surface Mo. To prepare pairs of surfaces that were identical in the step configuration, impurity concentration, and extended defect population, we cleaved single crystals to produce two mated surfaces which are mirror images. To test the reliability of this procedure, we reacted two halves of the same crystal with MeOH saturated  $\text{N}_2$  at the same time and found that the size and density of the  $H_x\text{MoO}_3$  precipitates in mirrored areas were identical. In fact, we found that when any two fresh crystals were treated in the reactor at the same time, the  $H_x\text{MoO}_3$  precipitate densities in the center of the (010) facet were comparable. In the experiments described in this section, the reactions with MeOH were always carried out on two halves of the same crystal. However, pits were introduced differently on the two halves so that they had different populations of undercoordinated surface Mo.

The image in Fig. 5 shows a surface that was first reduced in forming gas for 4 min at 400°C to introduce pits, and then

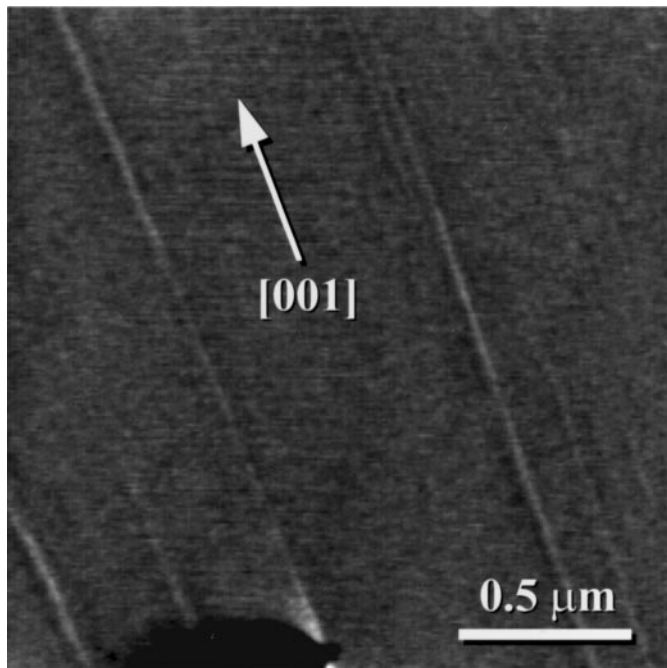


FIG. 4. Contact AFM image showing the intersection of pits with the surface/CS plane intersections formed during reduction in forming gas at 400°C. The heights of the steps (white contrast) emerging from the pit (black contrast) are approximately 2 Å.

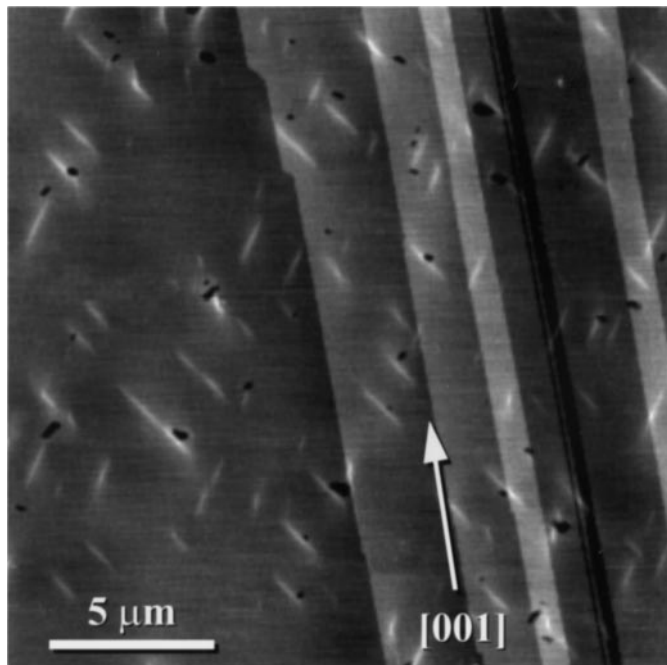


FIG. 5. AFM topograph of a  $\text{MoO}_3(010)$  surface which was reduced for 4 min at  $400^\circ\text{C}$  in  $10\%\text{H}_2\text{-N}_2$  and then reacted for 15 min at  $300^\circ\text{C}$  in  $\text{N}_2$  saturated with  $\text{MeOH}$  at  $0^\circ\text{C}$ . The largest  $\text{H}_x\text{MoO}_3$  precipitates are localized at the pits introduced during reduction. The black-to-white contrast in the image is  $40 \text{ \AA}$ .

reacted at  $300^\circ\text{C}$  for 15 min in  $\text{N}_2$  saturated with  $\text{MeOH}$  at  $0^\circ\text{C}$ . The  $\text{H}_x\text{MoO}_3$  precipitates on this surface are clustered around the surface pits introduced during reduction. In most cases, the largest precipitates intersect a pit or are very near a pit, while the pit-free areas have few or very small precipitates. The control half of this crystal was not reduced in the forming gas and had a relatively flat surface. Although it was reacted with  $\text{MeOH}$  alongside the pitted crystal, no  $\text{H}_x\text{MoO}_3$  was detected in mirrored areas of the flat crystal.

With longer reaction times, very large  $\text{H}_x\text{MoO}_3$  precipitates grow from the pits and extend into the  $\text{MoO}_3$  matrix. The image in Fig. 6a shows a surface that was reduced for 10 min at  $400^\circ\text{C}$  in forming gas, reoxidized for 2 h at  $400^\circ\text{C}$  in the ambient, and, finally, reacted for 20 min at  $330^\circ\text{C}$  in  $\text{N}_2$  saturated with  $\text{MeOH}$  at  $0^\circ\text{C}$ . The enhanced formation of  $\text{H}_x\text{MoO}_3$  at the pit edges is obvious. Although smaller precipitates can also be found on the surface, the largest precipitates always originate at a pit. The other half of this crystal was not reduced in forming gas, but was annealed in air and  $\text{MeOH}$  with the pitted crystal. A mirrored area of this surface is shown in Fig. 6b. On this flat surface, the precipitates are more numerous, but much smaller. The average height of the precipitates on the pitted surface is  $43 \text{ \AA}$  while the average height on the flat surface is only  $6 \text{ \AA}$ . The volume of  $\text{H}_x\text{MoO}_3$  per surface area is  $1 \times 10^{-6} \text{ cm}$  on the

pitted surface and  $1 \times 10^{-7} \text{ cm}$  on the flat surface. Thus, the surface with pits intercalated 10 times more hydrogen than the flat surface.

A similar effect is observed on surfaces oxidized for longer times to produce larger, rectangular pits. For

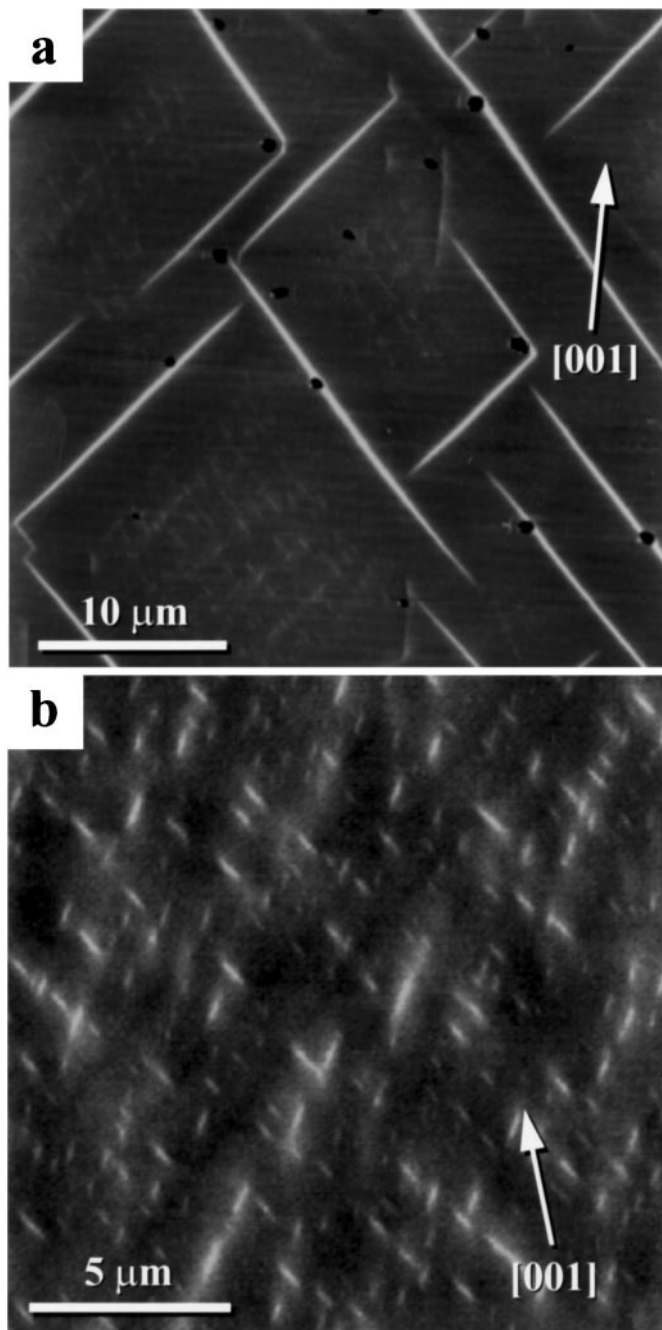
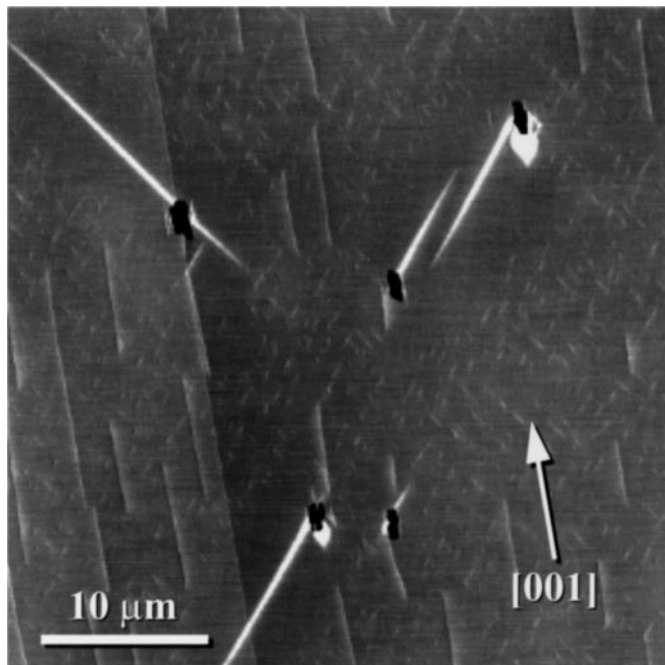


FIG. 6. AFM topographs of mirrored areas of pitted (a) and flat (b)  $\text{MoO}_3(010)$  surfaces reacted for 20 min at  $330^\circ\text{C}$  in  $\text{N}_2$  saturated with  $\text{MeOH}$ . The pitted surface was reduced for 10 min at  $400^\circ\text{C}$  in forming gas and then oxidized for 2 h at  $400^\circ\text{C}$  in the ambient prior to the  $\text{MeOH}$  reaction. The volume of  $\text{H}_x\text{MoO}_3$  per surface area is  $10^{-6} \text{ cm}$  on the pitted surface and  $10^{-7} \text{ cm}$  on the flat surface. The black-to-white contrast in (a) and (b) is 100 and 20  $\text{ \AA}$ , respectively.



**FIG. 7.** AFM topograph of a  $MoO_3(010)$  surface that was reduced in forming gas at  $400^\circ C$  for 10 min, oxidized for 3 h at  $410^\circ C$  in air, and then exposed to  $N_2$  saturated with MeOH for 15 min at  $330^\circ C$ . The black-to-white contrast in the image is 100 Å.

example, the image in Fig. 7 is of a surface that was reduced in forming gas at  $400^\circ C$  for 10 min and then oxidized for 3 h at  $410^\circ C$  in the ambient. Finally, it was exposed to  $N_2$  saturated with MeOH at  $25^\circ C$  for 15 min at  $330^\circ C$ . While most of the surface is covered with small  $H_xMoO_3$  precipitates, very large ones grow from the pit edges and extend into the matrix of the crystal.

Through the oxidation treatments, we can exercise some control over the size and the shape of the surface pits. As an example, two halves of the same crystal were reduced for 5 min at  $400^\circ C$  in forming gas. One half was then oxidized in ambient air at  $410^\circ C$  for 1 h while the other half simply remained at room temperature. The surfaces were then reacted for 10 min at  $330^\circ C$  in  $N_2$  saturated with MeOH at room temperature. Characteristic AFM images from the same regions of the two surfaces are shown in Fig. 8. The pits shown in Fig. 8a are all less than 200 Å deep. On the other hand, the pits on the surface that received the oxidation treatment are all greater than 500 Å deep (see Fig. 8b). The  $H_xMoO_3$  precipitates on the surface with the larger pits (Fig. 8b) are larger and more numerous than those on the surface with more shallow pits (Fig. 8a). Furthermore, the calculated volumes of  $H_xMoO_3$  per area on the surfaces with the shallow and deep pits are  $5 \times 10^{-7}$  and  $2 \times 10^{-6}$  cm, respectively. Finally, note that as the density of pits is increased and the distance between adjacent pits becomes smaller, the preferential nucleation at particular pits is less pronounced. A similar effect is also observed on (010) sur-

faces with large populations of rectangular pits formed by reoxidation.

### (c) The Effect of Lateral Facets

As mentioned in the introduction, steps and pits on the (010) surface introduce out of plane components where the

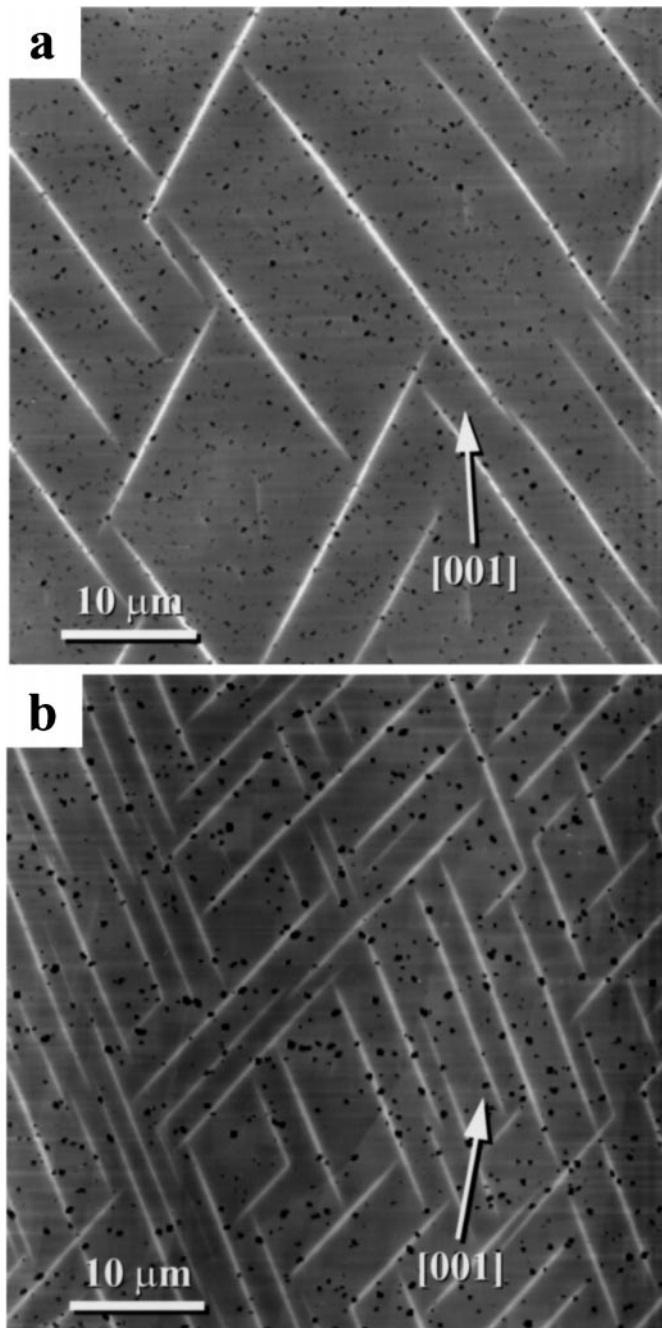


**FIG. 8.** AFM topographs illustrating the effect of pit size on  $H_xMoO_3$  precipitation during a 10-min reaction at  $330^\circ C$  with  $N_2$  saturated with MeOH. The calculated volumes of  $H_xMoO_3$  per surface area are  $5 \times 10^{-7}$  cm (a) and  $2 \times 10^{-6}$  cm (b). The black-to-white contrast in (a) is 200 Å, while that in (b) is 400 Å.

local bonding geometry should be similar or identical to that found on the lateral facets. Indeed, when regions of the (010) surface near the lateral facets are examined, it is clear that the rate of  $H_xMoO_3$  formation is enhanced. However, a number of qualifying statements should be made. First, the enhanced reaction from the crystal edges is observed only in the 100- $\mu\text{m}$ -thick region closest to the edge. The central regions have a uniform precipitate density that is unaffected by the proximity to the edges. So, while hydrogen is preferentially intercalated at the edges of the crystal, it also enters through the (010) surface, but at a slower rate. All of the images presented here were recorded in the central region of crystals with lateral dimensions greater than 1 mm and were not subject to edge effects.

For extended reaction times ( $t > 40$  min) at 330°C, a new precipitate morphology was observed (see Fig. 9a). The white contrast along the [001] axis in Fig. 9a corresponds to swollen surface regions that nucleate at {001} facets and grow until they extend several millimeters into the crystal. The surface relief over these features can be as high as 500 Å. The nucleation of these features can also be observed at large steps occasionally created by the cleavage process (see Fig. 9b). While large cleavage steps with heights greater than 500 Å behave as lateral facets, the enhanced reactivity is not obvious at the steps which are only a few unit cells in height.

All of the Bragg peaks in X-ray powder diffraction patterns of surface layers removed from crystals that contained the swollen [001] features could be assigned to  $MoO_3$  and  $H_xMoO_3$  ( $0.23 \leq x \leq 0.4$ ). Based on this, we assume that the swollen regions are simply a second habit that  $H_xMoO_3$  adopts as the volume fraction of precipitates dominates the matrix. In many cases, a crack propagates along the axis of the swollen region. Cracks make the interior of the crystal accessible to MeOH and enable more layers to be transformed to  $H_xMoO_3$ , therefore leading to enhanced surface relief.

## DISCUSSION

The results presented above demonstrate that two halves of the same crystal, reacted together under the same conditions, intercalate different amounts of hydrogen if they have different surface topographies. We can be certain that the mated sample surfaces used for the comparisons were indistinguishable in the macroscopic structure of the basal plane, the impurity concentration, and the dislocation density. However, the procedures used to modify the surface topography and density of  $\{h0l\}$  sites also alter the absolute surface area of the basal plane and the stoichiometry of the sample. The magnitude of these changes and the potential effect that they might have on the formation of the intercalated phase are discussed below.

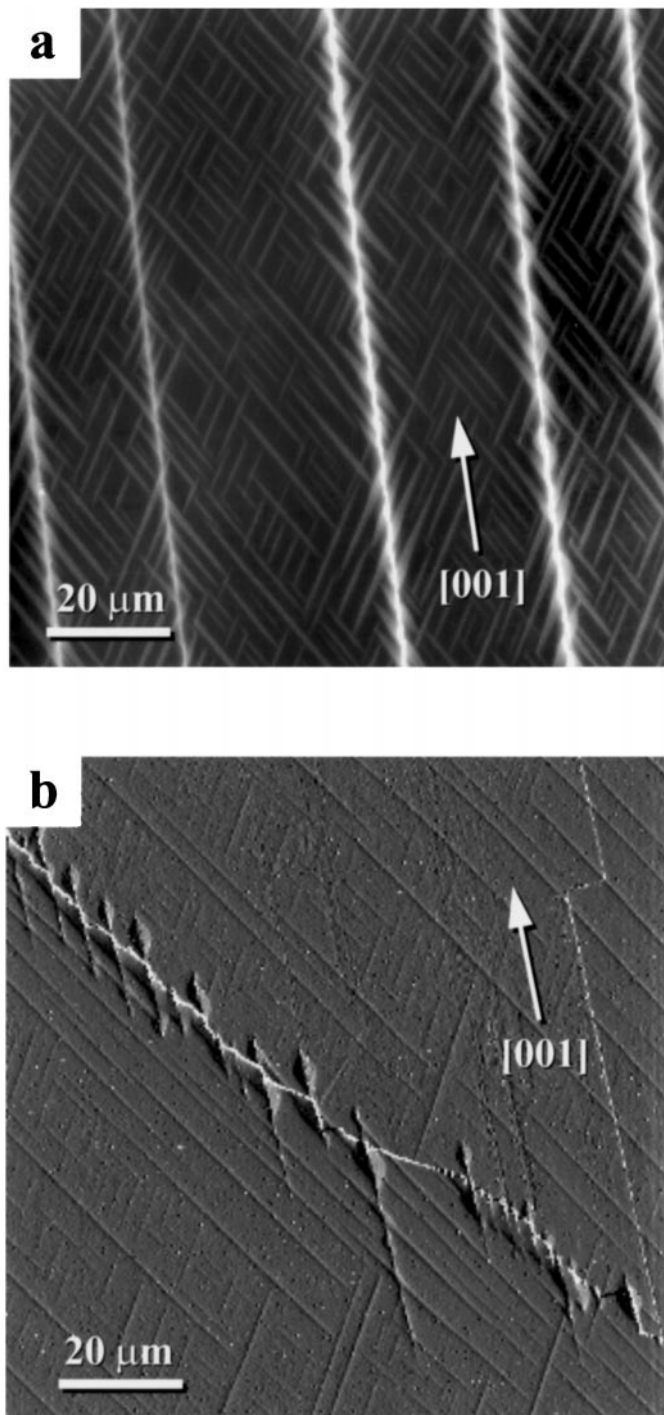


**FIG. 9.** (a) AFM topograph of a  $MoO_3(010)$  surface which was reacted for 30 min at 330°C in  $N_2$  saturated with MeOH. The black-to-white contrast in the image is 500 Å. The heights of the long, straight precipitates oriented along [001] are approximately 500 Å. (b) The [001] habit of  $H_xMoO_3$  forms preferentially at cleavage steps on the  $MoO_3(010)$  surface during reaction with MeOH- $N_2$  at 300°C. In this AFM deflection image, the step is the white line of contrast which extends diagonally across the image. The terrace below the edge in the image is topographically higher than the terrace above.

The changes in the absolute surface area can be estimated based on the AFM data. For example, the images in Fig. 6 show that the total volume of the bronze formed on the pitted surface is 10 times larger than that which is formed on the ideally flat surface. The basal component of the area in Fig. 6a is  $1.6 \times 10^{-9} \text{ m}^2$ . With AFM data, we can approximate the additional surface area contributed by the 17 pits in this area of the surface. Assuming that the pits are idealized right cylinders, the total  $\{h0l\}$  surface area is only  $4 \times 10^{-12} \text{ m}^2$ , about 0.3% of the total surface area. Based on these numbers, we can conclude that the order of magnitude increase in the amount of hydrogen intercalated by the pitted surface is not simply due to the increase in the surface area, but to the nature of the new surfaces.

By using mated halves of the same crystal and characterizing the size and density of pits formed on these surfaces, we have established experimental control of the density of undercoordinated Mo contributed by  $\{h0l\}$  facets. However, additional undercoordinated Mo are found next to vacant oxygen sites, the population of which is controlled by the temperature and partial pressure of oxygen in the reactor. Under the assumption that the surface plane responds to environmental changes rapidly, both halves of the crystal should have equal concentrations of surface oxygen vacancies during the final side-by-side reactions in MeOH. It might be argued, however, that if bulk oxygen diffusion determines the surface vacancy concentration, then surfaces reduced in forming gas to create pits are relatively enriched with surface oxygen vacancies and undercoordinated Mo with respect to the flat surfaces. When we consider the observations discussed in the last section, we conclude that this cannot be the case.

Consider, for example, the results depicted in Fig. 8. Both samples were initially reduced in forming gas to generate an identical pit distribution. At this stage, the vacancy concentration in the two samples should have been identical. One sample was then annealed in air to allow some enlargement of the pits. While this sample must have been relatively depleted of oxygen vacancies, it was observed to intercalate more hydrogen than the reduced sample. Therefore, the difference in the amount of hydrogen intercalated by the two samples does not correlate to the potential difference in the oxygen vacancy concentration. While vacant sites are probably active for methanol chemisorption, their relative concentration is apparently not high enough, even after reducing pretreatments, to greatly influence the amount of  $H_xMoO_3$  formed.

With this observation in mind, it is interesting to estimate possible ranges for the surface vacancy concentration. If we assume that the undercoordinated sites introduced by oxygen vacancies and step edges have the same reactivity, we can use our measured site density on pitted surfaces to place an upper limit on the vacancy concentration. For

example, consider the surfaces in Fig. 6. The introduction of pits (Fig. 6a) leads to the creation of  $4 \times 10^{-8} \text{ cm}^2$  of new surface area and, assuming that there are  $6.8 \times 10^{14} \text{ Mo/cm}^2$ , the exposure of  $2.7 \times 10^7$  new Mo sites. On a basal surface of the same area, there are  $8.3 \times 10^9$  Mo sites and 3 O sites for each Mo. Therefore, the vacancy concentration per surface oxygen site would have to be  $10^{-3}$  to expose the same number of Mo as the pits. Since the surface depicted in Fig. 6b intercalated less hydrogen than the one in Fig. 6a, we conclude that the concentration of undercoordinated Mo sites arising from oxygen vacancies was less than  $10^{-3}$  per oxygen site.

Similarly, the observation that hydrogen intercalation is enhanced by the relatively deep pits, large surface steps, and the lateral edges of the crystal, but not by single layer surface steps, can be used to place a lower limit on the vacancy concentration. Based on images of cleavage surfaces, we estimate that the typical density of undercoordinated Mo associated with small steps is on the order of  $10^{10}/\text{cm}^2$ . The equivalent concentration of undercoordinated basal plane sites can be created using a vacancy concentration per oxygen site of  $10^{-5}$ . Since  $H_xMoO_3$  is not observed to nucleate preferentially on the small step edges of a cleavage surface, we conclude that the vacancy concentration is greater than  $10^{-5}$ . It is gratifying to note that the oxygen vacancy concentration estimated by researchers in the past for similar experimental conditions is  $10^{-4}$  and that this figure falls between the limits implied by our observations (9, 10).

In summary, we can say that as the density of  $\{h0l\}$  surfaces increases,  $MoO_3$  intercalates more hydrogen. The observed increase in hydrogen uptake is much greater than can be explained by differences in the absolute surface area and does not correlate to potential differences in the surface vacancy concentration. This result, taken together with the observation that  $H_xMoO_3$  precipitates emerge from intentionally introduced and native  $\{h0l\}$  surfaces, leads us to conclude that the chemisorption properties of the  $\{h0l\}$  planes are much different than the  $\{010\}$  planes. These results are consistent with the idea that the active sites for dissociative chemisorption are the undercoordinated Mo sites that must exist on the  $\{h0l\}$  facets. While this result has already been reported for room temperature reactions with MeOH (1, 2), the current work illustrates that these sites are also active at typical reactor temperatures and pressures.

While the temperature programmed desorption studies reported by Farneth and co-workers (1, 2) and the AFM observations reported here lead to similar conclusions, we must also consider the Tatibouët and Germain (18) atmospheric pressure reactor study of catalyst particles with different morphologies. Their results indicated that the basal planes were responsible for formaldehyde formation, while the edge facets were responsible for the formation of higher order products such as dimethyl ether and

dimethoxy methane. It might be possible to reconcile these observations by assuming that the lateral facets provide sites for dissociative chemisorption and formation of the H-bronze phase, but that decomposition of the methoxy, which is rate limiting, requires the presence of the basal surface. If it is true that both types of surfaces are required for a selective reaction, then the basal facet alone would be inert, as reported by Farneth and coworkers (1, 2), while increasing the relative basal plane surface area in the presence of some lateral facets would enhance the concentration of products from the rate limiting step, as reported by Tatibouët and Germain (18).

#### ACKNOWLEDGMENT

This work was supported by the National Science Foundation under YIA Grant DMR-9458005.

#### REFERENCES

1. Farneth, W. E., Ohuchi, F., Staley, R. H., Chowdhry, U., and Sleight, A. W., *J. Phys. Chem.* **89**, 2493 (1985).
2. Farneth, W. E., Staley, R. H., and Sleight, A. W., *J. Am. Chem. Soc.* **108**, 2327 (1986).
3. Chung, J. S., Miranda, R., and Bennett, C. O., *J. Catal.* **114**, 398 (1988).
4. Machiels, C. J., and Sleight, A. W., in "Proceedings of the 4th International Conference on the Chemistry and Uses of Molybdenum" (H. F. Barry and P. C. H. Mitchell, Eds.), p. 411. Climax Molybdenum Co., Ann Arbor, MI, 1982.
5. Vergnon, P., and Tatibouët, J. M., *Bull. Soc. Chim. Fr.* **11-12**, 455 (1980).
6. Guidot, J., and Germain, J. E., *React. Kinet. Catal. Lett.* **15**, 389 (1980).
7. Smith, R. L., and Rohrer, G. S., *J. Catal.* **173**, 219 (1998).
8. Kihlberg, L., *Ark. Kemi.* **21**, 357 (1963).
9. Bursill, L. A., *Proc. R. Soc.* **A311**, 267 (1969).
10. Thöni, W., and Hirsch, P. B., *Phil. Mag.* **33**, 639 (1976).
11. Smith, R. L., and Rohrer, G. S., *J. Catal.*
12. Smith, R. L., and Rohrer, G. S., *J. Catal.* **163**, 12 (1996).
13. Smith, R. L., and Rohrer, G. S., in "Catalyst Materials for High-Temperature Processes" (K. S. Ramesh, M. Misono, and P. L. Gai, Eds.), Ceramic Transactions 73, p. 139, American Ceramic Society, Westerville, OH, 1997.
14. Smith, R. L., and Rohrer, G. S., *J. Solid State Chem.* **124**, 104 (1996).
15. Millner, T., and Neugebauer, J., *Nature* **163**, 601 (1949).
16. Belton, G. R., and Jordan, A. S., *J. Phys. Chem.* **69**, 2065 (1965).
17. Gai, P. L., and Labun, P. A., *J. Catal.* **94**, 79 (1985).
18. Tatibouët, J. M., and Germain, J. E., *J. Catal.* **72**, 375 (1981).